

Spin transistor built on 2D van der Waals heterostructures

Shengwei Jiang^{1,2}, Lizhong Li², Zefang Wang^{2,3}, Jie Shan^{1,2,4*}, and Kin Fai Mak^{1,2,4*}

¹Laboratory of Atomic and Solid State Physics, Cornell University, Ithaca, NY, USA

²School of Applied and Engineering Physics, Cornell University, Ithaca, NY, USA

³Department of Physics, Penn State University, University Park, PA, USA

⁴Kavli Institute at Cornell for Nanoscale Science, Ithaca, NY, USA

*E-mails: kinfai.mak@cornell.edu; jie.shan@cornell.edu.

Spin transistors (whose on-off operation is achieved by electric-field-controlled spin orientation ¹), if realized, can revolutionize modern electronics through the implementation of a faster and a more energy-efficient performance as well as non-volatile data storage ^{2,3}. The original proposal by Datta and Das ¹ that relies on electric-field-controlled spin precession in a semiconductor channel faces significant challenges including inefficient spin injection, spin relaxation and spread of the spin precession angle ^{4,5}. Recent demonstration of electric-field switching of magnetic order ⁶⁻⁸ and spin filtering ⁹⁻¹² in two-dimensional magnetic insulator CrI₃ has inspired a new operational principle for spin transistors. Here we demonstrate spin field-effect transistors based on dual-gated graphene/CrI₃ tunnel junctions. These devices show an ambipolar transistor behavior and tunnel magnetoresistance widely tunable by gating when the CrI₃ magnetic tunnel barrier undergoes an antiferromagnetic-ferromagnetic spin-flip transition. Under a constant magnetic bias in the vicinity of the spin-flip transition, the gate voltage can repeatedly alter the device between a high and a low conductance state with a large hysteresis. This new spin transistor concept based on the electric-field-controlled spin-flip transition in the magnetic tunnel barrier is immune to interface imperfections and allows spin injection, control and detection in a single device.

The discovery of two-dimensional (2D) magnetic crystals ¹³⁻²² has provided a unique platform to explore new spintronic device concepts with unprecedented controllability. CrI₃, a layered magnetic insulator ²³, has shown an intriguing layer thickness-dependent magnetic order ¹³: whereas monolayer CrI₃ is an Ising ferromagnet with spins pointing out-of-plane, bilayer CrI₃ is an antiferromagnet consisting of two ferromagnetic monolayers with antiparallel spins. Under a magnetic field of less than 1 T, bilayer CrI₃ can be turned into a ferromagnet through a spin-flip transition, suggesting an interlayer exchange interaction on the order of ~ 0.2 meV ⁷. Such a weak interlayer interaction opens the possibility of inducing the spin-flip transition by means other than a magnetic field. Indeed, recent experiments have demonstrated antiferromagnet-ferromagnet switching in bilayer CrI₃ by either a pure electric field ⁶ or electrostatic doping ^{7,8} under a constant magnetic bias. Another parallel recent advance in atomically thin magnetic crystals is the discovery of large tunnel magnetoresistance (TMR) in magnetic tunnel junctions utilizing 2D CrI₃ as a tunnel barrier ⁹⁻¹². Because of the efficient spin filtering effect in 2D CrI₃, a change in the tunnel resistance by $\sim 100\%$ has

been observed when bilayer CrI_3 undergoes an antiferromagnet-ferromagnet transition driven by an external magnetic field. Magnetoresistance thus provides an effective means to read the magnetic state of 2D CrI_3 . These two important results, when combined, provide the basis for a conceptually new spin transistor that we investigate in this study.

Our device consists of a van der Waals heterostructure of bilayer graphene/bilayer CrI_3 /bilayer graphene with top and bottom gates (Fig. 1a). See Methods for fabrication details and Supplementary Sections 1 and 2 for basic materials and device characterization. The vertical tunnel junction utilizes bilayer graphene as the source and drain contacts to achieve an ambipolar transistor as we demonstrate below, and bilayer CrI_3 , as the magnetic tunnel barrier. The two nearly symmetric gates are made of few-layer graphene gate electrodes and hexagonal boron nitride (hBN) gate dielectrics of ~ 20 nm. The gates tune the Fermi level of the nearest bilayer graphene contact effectively, which modulates the conductance of the junction through resonant tunneling^{24,25}. This effectively is a tunnel field-effect transistor (TFET). The gates can also cause a significant modulation in the tunnel conductance by inducing a spin-flip transition in bilayer CrI_3 ⁶⁻⁸. A spin-TFET action is thus realized through electrical switching of spins in the magnetic tunnel barrier (Fig. 1a). This is in contrast to the original spin field-effect transistor proposed by Datta and Das that relies on the gate-controlled spin precession in a semiconductor channel¹.

Figure 1b is the tunnel conductance G measured under a small bias (4 mV) as a function of top gate voltage V_{tg} in the absence of back gate voltage and external magnetic field. The measurement was performed at 4 K, at which bilayer CrI_3 is an antiferromagnet. Measurements at varying temperatures are included in Supplementary Sect. 3. Here an ambipolar transistor behavior with a zero conductance (*i.e.* off) state is observed for graphene tunnel junctions. This is a consequence of a sizable band gap opened in both bilayer graphene contacts^{26,27} by a build-in interfacial electric field from the asymmetric hBN/bilayer graphene/bilayer CrI_3 structure (no off state is observed when gapless monolayer graphene is used as contacts, see Supplementary Sect. 6). A detailed bias dependence measurement, combined with modeling of resonant tunneling in the heterostructure, shows that the gap is around 100 meV (see Supplementary Sect. 5). The result also shows that both bilayer graphene contacts are unintentionally p -doped (likely due to charge transfer to CrI_3). Since the top gate is effectively screened by the top graphene contact and the CrI_3 barrier, its effect on the bottom graphene contact is negligible. Similarly, the effect of the bottom gate on the top graphene contact is also negligible. This is clearly seen in our devices (Supplementary Fig. S3 and S7) and we will focus on the top gate below, which influences only the Fermi level of the top graphene contact.

The gate dependence of the tunnel conductance shows three distinct regions: p - p , p - i and p - n (denoting the doping type in the bottom and top bilayer graphene contact, respectively) from left to right in Fig. 1b. The insets illustrate the band alignments of the two graphene contacts and the tunnel barrier. In the p - i region, the tunnel junction is off since the Fermi level of the bottom graphene contact falls inside the gap of the top graphene contact and no state is available for resonant tunneling in the zero-bias limit. In

the p - n region, when the junction is forward biased, electrons tunnel from the conduction band on the n -side to the unoccupied states in the valence band on the p -side through the CrI_3 barrier (upper panel, Fig. 1c). The tunnel current I reaches a peak when the Fermi level on the n -side aligns with the valence band maximum on the p -side. Further increase in the bias voltage V_b decreases the tunnel current, which is more clearly seen in the negative differential conductance dI/dV_b (dip 1 in lower panel, Fig. 1c and inset). The negative differential conductance is the key signature of a p - n tunnel diode^{24, 25, 28}. In the p - p region, negative differential conductance disappears as expected. Instead, there appears a kink in the tunnel current, or equivalently, a dip in the differential conductance on each side of zero bias (Fig. 1d). The dip under reversed biasing (dip 3) corresponds to the Fermi level of the bottom graphene contact inside the gap of the top graphene contact. It shifts towards higher reversed bias voltages for lower Fermi energies (i.e. higher hole doping) in the top graphene contact. On the other hand, the dip under forward biasing (dip 2) depends weakly on V_{tg} since it corresponds to the Fermi level of the top graphene contact inside the gap of the bottom graphene contact, whose Fermi level is hardly affected by top gating. The behavior of dip 2 and 3 is switched when a bottom gate voltage V_{bg} is applied instead of the top gate voltage (Fig. 1e), which is consistent with the picture given above and confirms that the two gates are symmetric. The dispersion of the dip positions (1-3) with V_{tg} is summarized in Fig. 1f (symbols) and is in good agreement with the resonant tunneling model (solid lines, details presented in Supplementary Sect. 5).

Equipped with the above basic understanding of the operation of our TFET, we now examine its TMR in Fig. 2a. The upper panel compares the gate dependence of the tunnel conductance G under 0 T and 1 T and shows in general larger G 's at 1 T. Figure 2c and 2f are the detailed magnetic-field dependence of G for a representative gate voltage from the p - p and p - n region, respectively. The tunnel conductance exhibits a sharp jump around 0.5 T, which is associated with the spin-flip transition in bilayer CrI_3 (See Supplementary Fig. S4 for independent verification by magnetic circular dichroism). The transition field depends on gate voltage^{7, 8}, which is a key property to realize the spin TFET as we discuss below. The magnetic hysteresis reflects the first-order nature of the spin-flip transition²⁹. We calculate the $\text{TMR} = \frac{G_{FM} - G_{AFM}}{G_{AFM}}$ using the conductance at 0 T and 1 T for G_{AFM} and G_{FM} , respectively, in the lower panel of Fig. 2a. It is $\sim 80\%$ in the p - p and p - n regions and is weakly gate dependent. The TMR here is governed by the spin filtering efficiency of CrI_3 (the ratio of the transmission probability of electrons with spins parallel to antiparallel to magnetization in each CrI_3 monolayer), which can be estimated to be ~ 3.3 and is in good agreement with the reported values^{9, 10}. What's more interesting, however, is the behavior of TMR near the boundaries of the off state of the TFET. An enhancement is observed at the p - p and p - i boundary (Fig. 2d). The TMR even becomes negative with large amplitude at the p - i and p - n boundary, i.e. $G_{FM} < G_{AFM}$ (Fig. 2e). A careful examination of Fig. 2a indicates that the gate dependence of G_{FM} is shifted from that of G_{AFM} towards larger V_{tg} 's. Because of the ambipolar transistor behavior of the TFET, this shift leads to an enhancement of the TMR and a sign change at the boundaries of the off state. Such a behavior has been observed in all devices with the same structure studied in this work although the detailed values of the TMR vary

from device to device. Figure 2b is the result for device 2 showing peak TMR values of $\sim 1,000\%$ and $-10,000\%$ at the boundaries of the off state.

To understand the shift between the gate dependence of G_{AFM} and G_{FM} , we have performed detailed bias dependence measurements of the tunnel conductance under varying magnetic fields. Figure 3a and 3b are the differential conductance dI/dV_b as a function of bias voltage for a representative $p-n$ and $p-p$ junction, respectively. The curves under different magnetic fields ranging from -1 T to 1 T with a step of 0.1 T are vertically displaced for clarity. We track the position in bias voltage of differential conductance dip 1 - 3 as a function of magnetic field (Fig. 3c - 3e). All three dip positions show a clear jump across the spin-flip transition of bilayer CrI_3 with the ferromagnetic state occurring at a larger absolute bias. This jump can be understood as a downshift of the Fermi energy in the graphene contacts as a result of the spin-flip transition. For instance, the negative differential conductance for the $p-n$ junction (dip 1) upshifts by ~ 20 mV across the spin-flip transition (Fig. 3c). It corresponds to a downshift of the graphene Fermi level by ~ 20 meV (Fig. 2f). The downshift of the Fermi level is equivalent to having a higher unintentional hole doping density, thus shifting the gate dependence of G_{FM} towards larger V_{tg} 's. Figure 3c - 3e also show the gate dependence of the height of each jump and the absolute position of the dips, which are discussed in Supplementary Sect. 4. A plausible mechanism for the Fermi level shift is a magnetic order-dependent band structure in CrI_3 ³⁰. This can change the built-in electric field as well as charge transfer at the graphene/ CrI_3 interfaces. Such a picture is supported by the observed TMR with $G_{FM} > G_{AFM}$ away from the boundaries of the off state because spin filtering can also be viewed as a reduction in the tunnel barrier height for ferromagnetic CrI_3 ⁹⁻¹². Future theoretical studies with accurate band structure calculations are needed for a quantitative description of our observation. Nevertheless, we summarize in Fig. 2c-f schematically the graphene band alignments across the spin-flip transition and the corresponding behavior of TMR. In the $p-p$ and $p-n$ regions (Fig. 2c, 2f), TMR is originated from spin filtering, as reported by Ref.⁹⁻¹². Near the boundaries of the $p-i$ region (Fig. 2d, 2e), the significantly modified TMR is caused by a magnetic transition-induced Fermi level shift in the graphene contacts.

Finally we demonstrate the spin transistor action based on our TFET devices, *i.e.* control of the tunnel conductance G by electrically switching the magnetic order in the tunnel barrier. To minimize the trivial conductance change due to electrostatic doping, we choose a range of gate voltage from the $p-p$ region ($V_{tg} < 0$ V) where G is weakly gate dependent in the absence of magnetism. Figure 4a shows the gate dependence of G under a constant magnetic bias (-0.76 T), which is slightly above the spin-flip transition of bilayer CrI_3 under $V_{tg} = 0$ V. The gate voltage can repeatedly alter the TFET between a high (red symbols) and a low (black symbols) conductance state that have been achieved in Fig. 2 under 1 T and 0 T with the CrI_3 barrier in the ferromagnetic and antiferromagnetic state, respectively. A relative change of $\sim 35\%$ in the tunnel conductance has been achieved through gating and with a large hysteresis. The switching is originated from a gate-dependent spin-flip transition field, as discussed above. The relative change in the tunnel conductance can be significantly enhanced by using thicker tunnel barriers on the expense of the tunnel conductance. Figure 4b shows the action of a

spin-TFET with 4-layer CrI₃ barrier under a constant magnetic bias of -1.77 T (Supplementary Sect. 7 for additional characterizations of this device). Nearly 400% change in the tunnel conductance is achieved while the tunnel conductance is an order of magnitude lower than that in the spin-TFET with bilayer CrI₃ (Fig. 4a). In conclusion, we have demonstrated efficient electrical writing and readout of the magnetic states in a single spin-TFET device based on graphene-CrI₃ heterostructures. The device concept developed in this study will open up a new avenue for exploring power-efficient non-volatile memory devices based on electric-field controlled magnetism³¹.

Methods

Device fabrication. Van der Waals heterostructures of CrI₃, hexagonal boron nitride (hBN) and graphene were fabricated by the layer-by-layer dry transfer method³². Images of sample devices are shown in Supplementary Fig. S1. In this process, atomically thin samples of CrI₃, hBN and graphene were first exfoliated from their bulk crystals (HQ graphene) onto silicon substrates covered with a 300-nm thermal oxide layer. The thickness of thin flakes was initially estimated from their optical reflectance contrast on silicon substrates and later verified by the atomic force microscopy for hBN and few-layer graphene samples, and Raman spectroscopy for bilayer graphene. Bilayer CrI₃ was confirmed by the magnetization measurement under an out-of-plane magnetic field. The selected thin flakes of appropriate thickness and geometry were then picked up one-by-one by a stamp consisting of a thin layer of polycarbonate (PC) on polydimethylsiloxane (PDMS). The complete stack was then deposited onto substrates with pre-patterned Au electrodes. The residual PC on the device surface was dissolved in chloroform before measurements. Since atomically thin CrI₃ is extremely air sensitive, it was handled in a nitrogen gas environment with less than one-part-per-million oxygen and moisture inside a glovebox and was removed from the glovebox only after being fully encapsulated.

Electrical characterization. The device characterization was carried out in an Attocube closed-cycle cryostat (attoDry1000) down to 4 K and up to 2.5 T. The tunnel conductance of the graphene/CrI₃ tunnel junctions was measured by biasing CrI₃ using the bilayer graphene source and drain contacts (Fig. 1a). The bias voltage was kept in the low bias regime (4 mV in amplitude). For the magnetic field and gate voltage dependence studies of the tunnel conductance, the bias was modulated at a relatively low frequency of about 17 Hz and the resultant current was measured with a lock-in amplifier to reduce noise. The tunnel conductance was calculated as the ratio of current to bias. The bias dependence of the tunnel current was studied by applying a dc bias voltage using a sourcemeter and measuring the resultant dc current using a current preamplifier. The differential conductance as a function of bias voltage was obtained via numerical differentiation of the bias dependence of the tunnel current.

Magnetic circular dichroism. The magnetization of CrI₃ was characterized by magnetic circular dichroism (MCD) using a HeNe laser at 633 nm. An objective of numerical aperture 0.8 was used to focus the excitation beam to a sub-micron spot size on the devices. The optical power on the devices was limited to 5 μ W. The reflected light from the devices was collected by the same objective and detected by a photodiode. The

helicity of the optical excitation was modulated between left and right by a photoelastic modulator at 50.1 kHz. The MCD was determined as the ratio of the ac component (measured by a lock-in amplifier) to the dc component (measured by a multimeter) of the reflected light intensity.

References

1. Datta, S. & Das, B. Electronic analog of the electro-optic modulator. *Applied Physics Letters* **56**, 665-667 (1990).
2. Žutić, I., Fabian, J. & Das Sarma, S. Spintronics: Fundamentals and applications. *Reviews of Modern Physics* **76**, 323-410 (2004).
3. Awschalom, D.D. & Flatté, M.E. Challenges for semiconductor spintronics. *Nature Physics* **3**, 153 (2007).
4. Koo, H.C. et al. Control of Spin Precession in a Spin-Injected Field Effect Transistor. *Science* **325**, 1515 (2009).
5. Chuang, P. et al. All-electric all-semiconductor spin field-effect transistors. *Nature Nanotechnology* **10**, 35 (2014).
6. Jiang, S., Shan, J. & Mak, K.F. Electric-field switching of two-dimensional van der Waals magnets. *Nature Materials* **17**, 406-410 (2018).
7. Jiang, S., Li, L., Wang, Z., Mak, K.F. & Shan, J. Controlling magnetism in 2D CrI₃ by electrostatic doping. *Nature Nanotechnology* **13**, 549-553 (2018).
8. Huang, B. et al. Electrical control of 2D magnetism in bilayer CrI₃. *Nature Nanotechnology* **13**, 544-548 (2018).
9. Song, T. et al. Giant tunneling magnetoresistance in spin-filter van der Waals heterostructures. *Science* (2018).
10. Klein, D.R. et al. Probing magnetism in 2D van der Waals crystalline insulators via electron tunneling. *Science* (2018).
11. Wang, Z. et al. Very large tunneling magnetoresistance in layered magnetic semiconductor CrI₃. *Nature Communications* **9**, 2516 (2018).
12. Hyun Ho Kim et al. One million percent tunnel magnetoresistance in a magnetic van der Waals heterostructure. *arXiv:1804.00028* (2018).
13. Huang, B. et al. Layer-dependent ferromagnetism in a van der Waals crystal down to the monolayer limit. *Nature* **546**, 270 (2017).
14. Gong, C. et al. Discovery of intrinsic ferromagnetism in two-dimensional van der Waals crystals. *Nature* **546**, 265 (2017).
15. Yao, T., Mason, J.G., Huiwen, J., Cava, R.J. & Kenneth, S.B. Magneto-elastic coupling in a potential ferromagnetic 2D atomic crystal. *2D Materials* **3**, 025035 (2016).
16. Lee, J.-U. et al. Ising-Type Magnetic Ordering in Atomically Thin FePS₃. *Nano Letters* **16**, 7433-7438 (2016).
17. Bonilla, M. et al. Strong room-temperature ferromagnetism in VSe₂ monolayers on van der Waals substrates. *Nature Nanotechnology* **13**, 289-293 (2018).
18. O'Hara, D.J. et al. Room Temperature Intrinsic Ferromagnetism in Epitaxial Manganese Selenide Films in the Monolayer Limit. *Nano Letters* **18**, 3125-3131 (2018).

19. Du, K.-z. et al. Weak Van der Waals Stacking, Wide-Range Band Gap, and Raman Study on Ultrathin Layers of Metal Phosphorus Trichalcogenides. *ACS Nano* **10**, 1738-1743 (2016).
20. Zhou, B. et al. Possible structural transformation and enhanced magnetic fluctuations in exfoliated α -RuCl₃. *Journal of Physics and Chemistry of Solids* (2018).
21. Wang, Z. et al. Electric-field control of magnetism in a few-layered van der Waals ferromagnetic semiconductor. *Nature Nanotechnology* **13**, 554-559 (2018).
22. Yujun Deng et al. Gate-tunable Room-temperature Ferromagnetism in Two-dimensional Fe₃GeTe₂. *arXiv:1803.02038* (2018).
23. McGuire, M.A. Crystal and Magnetic Structures in Layered, Transition Metal Dihalides and Trihalides. *Crystals* **7**, 121 (2017).
24. Britnell, L. et al. Field-Effect Tunneling Transistor Based on Vertical Graphene Heterostructures. *Science* **335**, 947 (2012).
25. Britnell, L. et al. Resonant tunnelling and negative differential conductance in graphene transistors. *Nature Communications* **4**, 1794 (2013).
26. Zhang, Y. et al. Direct observation of a widely tunable bandgap in bilayer graphene. *Nature* **459**, 820 (2009).
27. McCann, E. Asymmetry gap in the electronic band structure of bilayer graphene. *Physical Review B* **74**, 161403 (2006).
28. Esaki, L. New Phenomenon in Narrow Germanium p-n Junctions. *Physical Review* **109**, 603-604 (1958).
29. Stryjewski, E. & Giordano, N. Metamagnetism. *Advances in Physics* **26**, 487-650 (1977).
30. Jiang, P., Li, L., Liao, Z., Zhao, Y.X. & Zhong, Z. Spin Direction-Controlled Electronic Band Structure in Two-Dimensional Ferromagnetic CrI₃. *Nano Letters* **18**, 3844-3849 (2018).
31. Matsukura, F., Tokura, Y. & Ohno, H. Control of magnetism by electric fields. *Nature Nanotechnology* **10**, 209 (2015).
32. Wang, L. et al. One-Dimensional Electrical Contact to a Two-Dimensional Material. *Science* **342**, 614 (2013).

Figures and figure captions

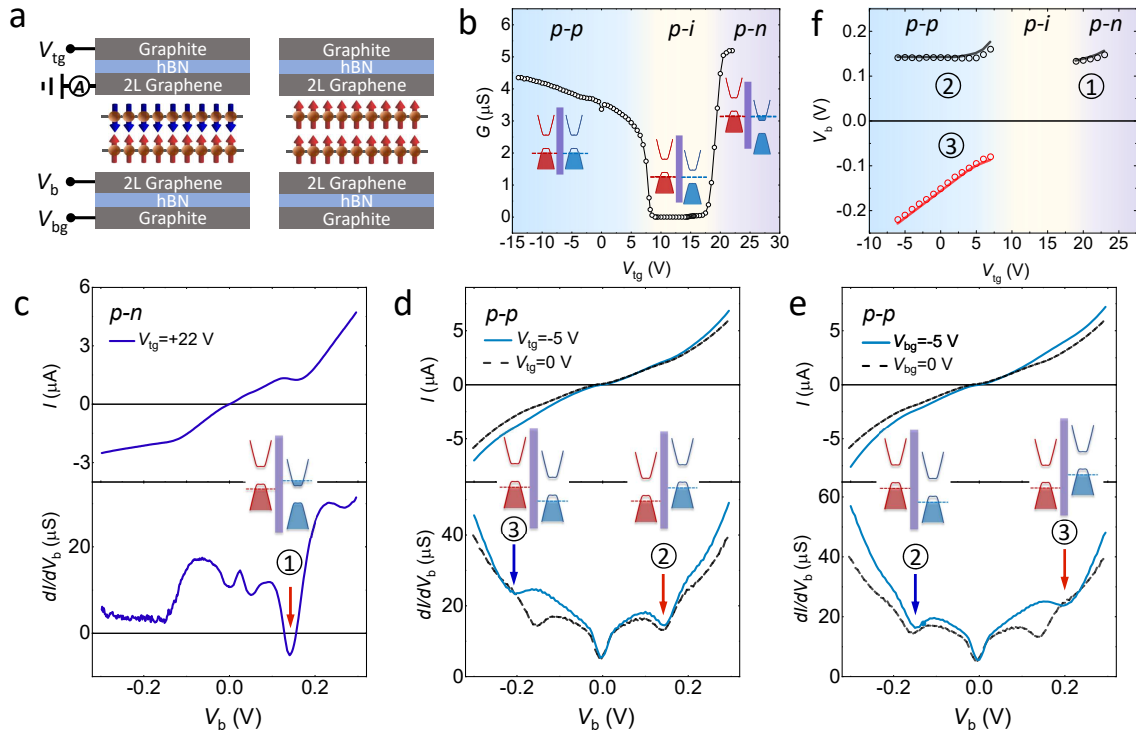


Figure 1 | Tunnel field-effect transistor (TFET) based on graphene/CrI₃ heterostructures. **a**, Operational principle of a spin TFET based on gate-controlled spin-flip transition in bilayer CrI₃ and spin filtering in the tunnel junction. Arrows indicate the spin orientation in CrI₃ layers. The left and right panels correspond to a low and a high tunnel conductance state, respectively. **b**, Gate dependence of tunnel conductance shows *p-p*, *p-i* and *p-n* regions. The feature at zero gate voltage is due to the resistance of the graphene contact in series with the tunnel junction. **c**, **d**, Bias dependence of tunnel current (upper panel) and differential conductance (lower panel) for representative *p-n* (**c**) and *p-p* (**d**) junctions. **e**, Same as **d** under a bottom instead of a top gate voltage. **f**, Gate dependence of bias voltages that correspond to differential conductance dip 1 - 3 as defined by arrows in **c** and **d**. The insets in **b** - **e** show the band alignments of the bottom (red) and top (blue) bilayer graphene contacts and the CrI₃ barrier (purple). Shaded areas are filled states.

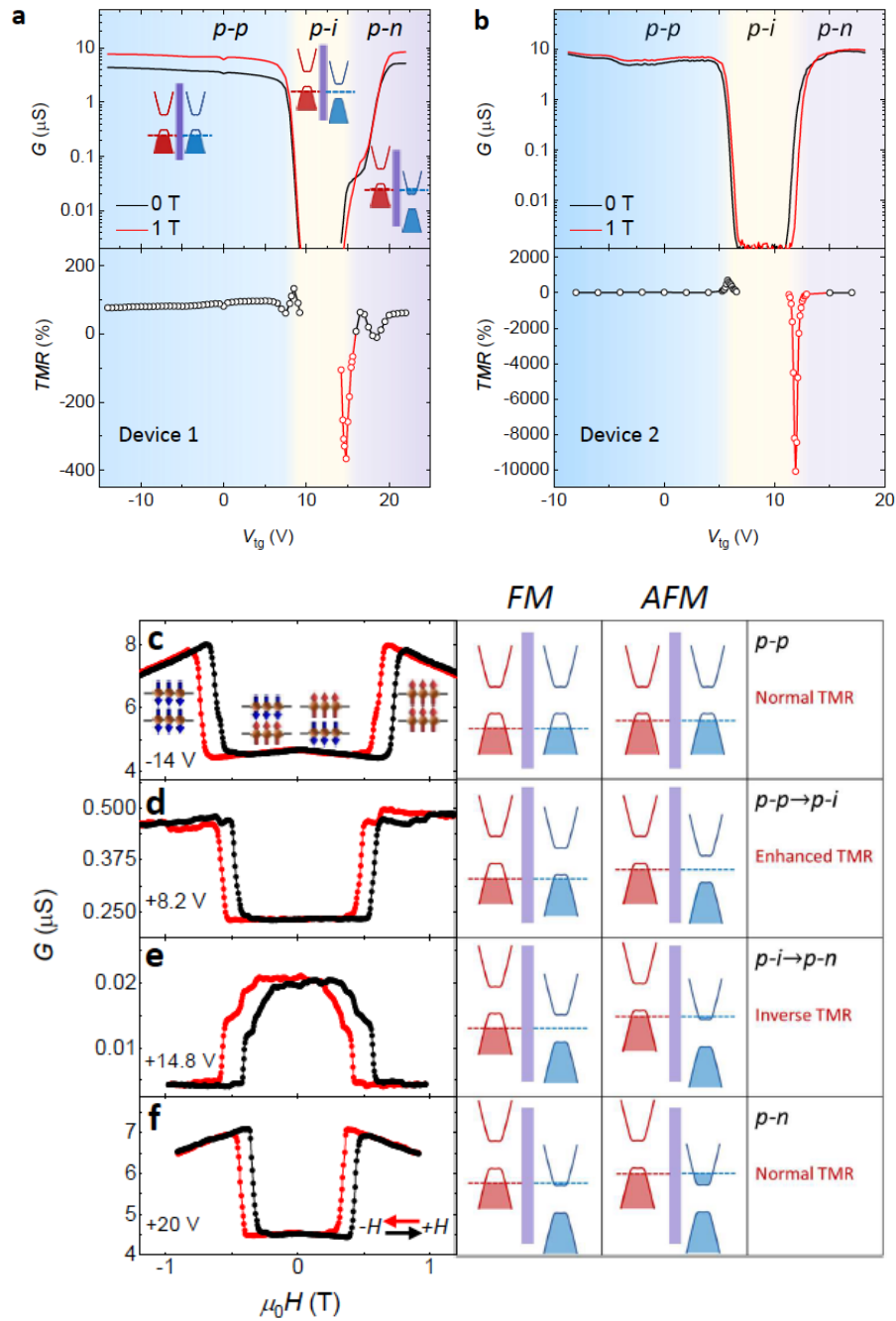


Figure 2 | Tunable tunnel magnetoresistance (TMR). **a**, Gate dependence of tunnel conductance under an out-of-plane magnetic field of 0 T and 1 T (upper panel), and TMR (lower panel) calculated from the values in the upper panel for device 1. The black and red symbols denote, respectively, the positive and negative values for TMR. The insets show the band alignments of the *p-p*, *p-i* and *p-n* tunnel junctions. **b**, Same as **a** for device 2. **c – f**, The left column is the magnetic-field dependence of tunnel conductance at varying top gates; middle two columns, the band alignments of the junction when CrI₃ is in the ferromagnetic (FM) and antiferromagnetic (AFM) state; right column, the behavior of TMR in the *p-p* (**c**), boundaries of *p-i* (**d**, **e**), and *p-n* (**f**) region.

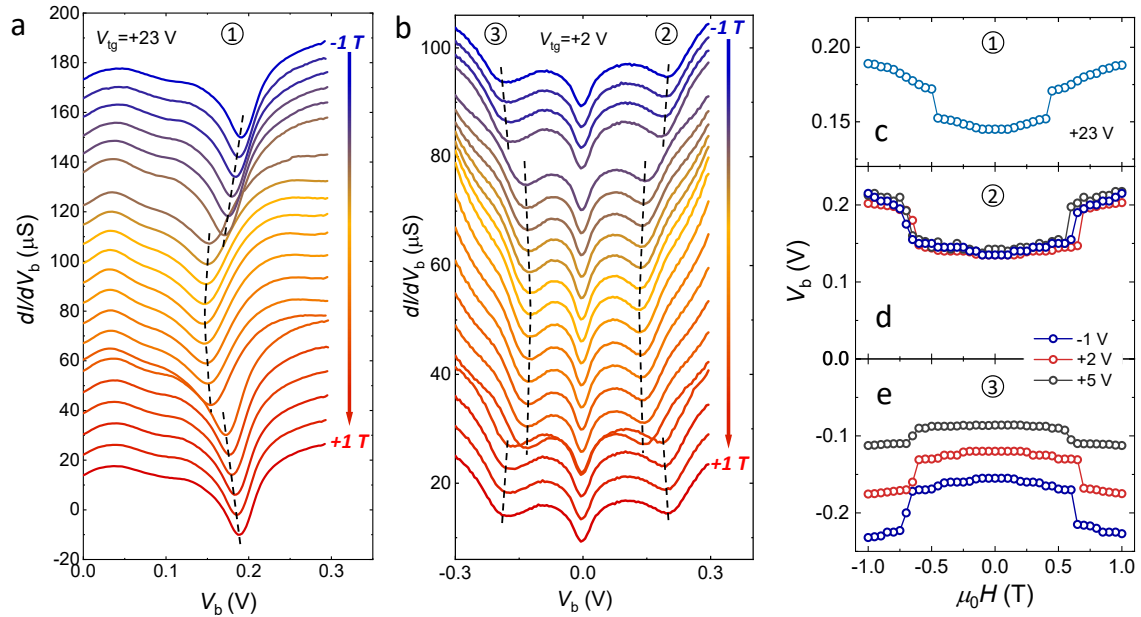


Figure 3 | Magnetic transition-induced band shift. **a, b**, Bias dependence of differential tunnel conductance of device 1 for a representative p - n (**a**) and p - p (**b**) junction. Results for magnetic field varying from 1 T to -1 T with a step size of 0.1 T are vertically displaced by the same amount for clarity. The dashed lines are guides to the eye for the evolution of differential conductance dip 1 (**a**) and dip 2 and 3 (**b**) as defined in Fig. 1c and 1d. **c - e**, Magnetic-field dependence of bias voltage corresponding to dip 1 (**c**), 2 (**d**) and 3 (**e**) for representative top gate voltages. The magnetic field was scanned from -1 T to 1 T.

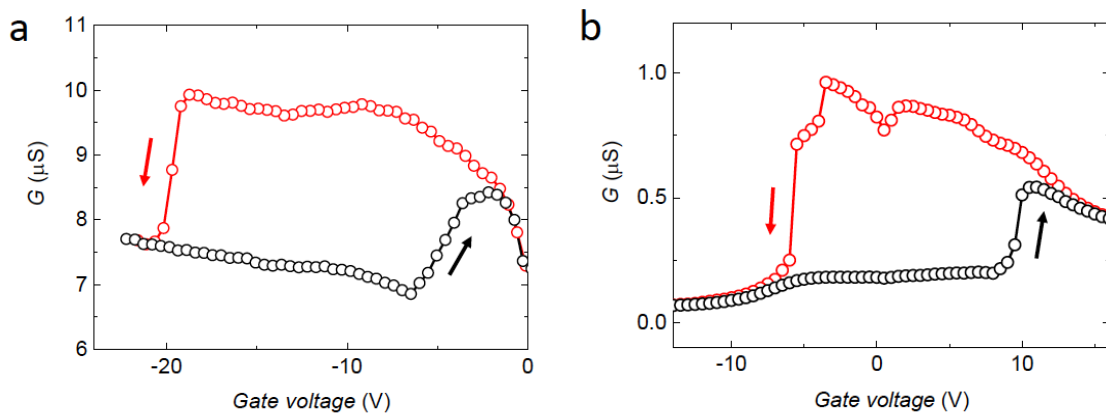


Figure 4 | Spin TFET action. **a**, Tunnel conductance of a TFET with a bilayer CrI_3 tunnel barrier is repeatedly switched by gating under a constant magnetic bias of -0.76 T. The top and bottom gate voltages are identical and their sum is shown in the horizontal axis. Black and red symbols correspond to measurements while sweeping the gate voltage forward and backward, respectively. A change of $\sim 35\%$ is seen in the tunnel conductance. **b**, The same as in **a** for a TFET with a four-layer CrI_3 tunnel barrier under a constant magnetic bias of -1.77 T. A change of $\sim 400\%$ is seen in the tunnel conductance.